Ceramics International 50 (2024) 14697–14707

Contents lists available at ScienceDirect

Ceramics International

journal homepage: www.elsevier.com/locate/ceramint

Structural, thermal, magnetic and microwave-absorbing properties of spinel-structured high entropy oxide $(MnFeCoNiX)_3O_4$ (X = Zn, Cu, Cr)

Jiaolong Du [a], Shen Bao [a], Wei Li [b,**], Yongqiang Chen [a], Bingbing Fan [a,c,*]

[a] School of Materials Science and Engineering, Zhengzhou University, Zhengzhou, 450001, China
[b] Department of Materials and Earth Sciences, Technical University of Darmstadt, Darmstadt, 64287, Germany
[c] College of Engineering, Mathematics and Physical Sciences, University of Exeter, Exeter City, EX4 4QF, United Kingdom

ARTICLE INFO

Handling Editor: Dr P. Vincenzini

Keywords:
High entropy oxide (HEO)
Magnetic properties
Electromagnetic (EM) microwave absorption
High-temperature resistance

ABSTRACT

Within the present work, a series of spinel-structured $(MnFeCoNiX)_3O_4$ (X = Zn, Cu, Cr) high entropy oxides (HEOs) were fabricated by co-precipitation method and the subsequent heat treatment. The phase composition, microstructure, thermal stability, magnetic property and electromagnetic (EM) wave loss ability were comprehensively studied. It is found that spinel-structural $(MnFeCoNiX)_3O_4$ HEOs are well-crystallized at above 800 °C with a space group Fd-3m. Morphological analysis reveals that grains of different HEOs contain nano-domains with particle sizes between 100 nm and 500 nm. In addition, Mn, Ni, Co, Fe, Zn, Cr and Cu elements are homogeneously distributed and the chemical states of Mn, Ni, Co and Fe are all +2 and + 3, while Cu only exists in +2 state. Thermal stability analysis shows that $(MnFeCoNiCu)_3O_4$ HEO is able to keep stable at 1000 °C. Moreover, the $(MnFeCoNiCu)_3O_4$ sample exhibits the best magnetic properties and EM microwave loss ability in comparison with $(MnFeCoNiZn)_3O_4$ and $(MnFeCoNiCr)_3O_4$. For $(MnFeCoNiCu)_3O_4$, the values of saturation magnetization (M_s) and coercivity (H_c) are 38.6 emu/g and 52.6 Oe, respectively. Meanwhile, $(MnFeCoNiCu)_3O_4$ displays a minimum reflection loss (RL) of −15.5 dB at 8.48 GHz with a thickness of 4.5 mm and a wide effective absorption bandwidth (EAB) of 8.84 GHz with the sample thickness of 5 mm. It is expected that the excellent high-temperature stability and good EM wave absorbing performance of high entropy $(MnFeCoNiCu)_3O_4$ could make it potentially useful in EM wave absorption under elevated temperatures.

1. Introduction

Adopting from the concept of high entropy alloys (HEAs), the high-entropy concept has been applied to a wide range of compounds, including oxides [1,2], carbides [3], borides [4,5], silicides [6], and others. HEAs are a kind of novel multi-component alloy that comprises five or more elements with an atomic concentration of 5–35 % [7,8]. Similarly, high-entropy oxides (HEOs) include a broad range of oxides that consist of five or more multi-principal cations with 5–35 % atomic composition [9,10]. Generally, HEOs with multi-cations distributed at various ionic states can demonstrate high-entropy effects on microstructural lattice distortion and kinetically sluggish diffusion, which could produce grain refinement and provide high-temperature stability [11,12]. In addition, the "cocktail effect" of multi-component solid solution phases is commonly seen in HEOs, which may lead to a combination of unpredictable properties in the final products [13]. Currently, the field of HEOs has attracted significant attention after the preparation of $(Mg_{0.2}Co_{0.2}Ni_{0.2}Cu_{0.2}Zn_{0.2})O$ featuring a single rock-salt phase by Rost et al. By choosing various cations and adjusting the composition of specific components, researchers have synthesized a variety of single-phase HEOs systems, such as (Co,Cu,Mg,Ni,Zn)O HEOs with rock-salt structure [14], rare earth doped $RE_2TM_2O_7$ HEOs with fluorite phase [15,16], $Sr(Zr,Sn,Ti,Hf,Mn)O_3$ HEOs with single-phase perovskite structure [17], high-entropy rare-earth silicates [18,19], Co–Cr–Fe–Mg–Mn–Ni–O HEO system with sing-phase spinel structure [20] and so on.

As one important kind of HEOs, MFe_2O_4 (M = Fe, Co, Cu, Zn, Ni, etc.) ferrites have drawn broad interest from researchers due to their special spinel crystalline structure with cations located in different intergranular intervals in face-centered cubic (fcc) oxygen lattice and various favorable properties, such as good thermal/chemical stability, magnetic, electrical properties and attractive electromagnetic (EM) performance

* Corresponding author. School of Materials Science and Engineering, Zhengzhou University, Zhengzhou, 450001, China.
** Corresponding author.
E-mail addresses: wei.li@stud.TU-Darmstadt.de (W. Li), fanbingbing@zzu.edu.cn (B. Fan).

https://doi.org/10.1016/j.ceramint.2024.01.383
Received 24 November 2023; Received in revised form 16 January 2024; Accepted 28 January 2024
Available online 29 January 2024
0272-8842/© 2024 Elsevier Ltd and Techna Group S.r.l. All rights reserved.

[21,22]. Usually, the synthetic strategies of spinel structured MFe_2O_4 are facile and cost-effective, including hydrothermal method [23–25], co-precipitation method and electrospinning method. And due to the aforementioned advantageous characteristics, MFe_2O_4 ferrites show great potential in the field of supercapacitors, catalysts, gas sensors and electromagnetic wave absorbers [26–28]. Particularly, spinel MFe_2O_4 ferrites as EM wave absorbing materials have been extensively researched in the last several years, owing to their intrinsic anisotropy, good dielectric capacity and high electric resistivity [29,30]. Radoń et al. synthesized one kind of (Zn,Mg,Ni,Fe,Cd)Fe_2O_4 high entropy ferrite by co-precipitating amorphous precursor and heat treatment and the results accentuated that the high entropy ferrite exhibited the excellent microwave absorption performance in the 1.9–2.1 GHz frequency range with the layer thickness of 0.8–1 cm [31]. In another research conducted by Mandal et al. transition metal-based MFe_2O_4 (M = Mn, Fe, Co, Ni, Cu, Zn) nano-hollow spheres were synthesized via one-pot template-free solvothermal technique [32]. Compared with traditional magnetite, the spinel-structured MFe_2O_4 displayed enhanced EM absorption properties as a result of M^{2+} [M = Mn, Co, Ni, Cu, Zn] substitution in Fe_3O_4, demonstrating prominent impedance matching, favorable dielectric and magnetic loss. Recently in 2022, Ma et al. reported that single phase spinel-type MFe_2O_4 (M = Mg, Mn, Fe, Co, Ni, Cu, Zn) high-entropy ferrites with synergetic dielectric and magnetic loss were synthesized by solid-state reaction method [33]. It was found that magnetic components are responsible for the enhanced magnetic loss ability and nano domains within the MFe_2O_4 grains as well as the hopping mechanism of resonance effect and high-entropy effect lead to improved dielectric properties, resulting in excellent EM absorbing properties. Although many spinel-structured MFe_2O_4 HEOs with magnetic and dielectric properties were investigated in the past several years, the system of MFe_2O_4 HEOs as EM microwave absorbers under high temperatures still needs to be broadened. Furthermore, high-temperature stabilities of the MFe_2O_4 HEOs are rarely mentioned in most of the previous researches.

Derived from the research experience of the HEA system, in the binary subsystem, the corresponding oxides of each of the eight elements (Co, Cr, Cu, Fe, Mg, Mn, Ni, Zn) have similarities in crystal structure, ionic radius, equivalence, and solubility, which are the dominant materials for the development of HEOs [34]. Specifically, based on the design inspiration of the cation substitution in high-entropy ceramics [35,36], and the methods of optimizing the exchange coupling at ferromagnetic interfaces [33,37], the controllable regulation of the magnetic properties of the HEOs is achieved by adjusting the cationic compositions of Zn, Cu, and Cr in the present experiments, and then realizing the effective combination of dielectric loss and magnetic loss of wave-absorbing materials. Therefore, three kinds of high-entropy spinel-type $(MnFeCoNiX)_3O_4$ (X = Zn, Cu, Cr) were synthesized by conventional chemical co-precipitation method, followed by calcination of the as-prepared precursors. The effects of calcination temperature on the phase composition and morphology evolution of different HEOs were investigated. High-temperature stability of the HEOs was also evaluated above 900 °C. Finally, the magnetic properties and EM microwave absorbing performance of the HE $(MnFeCoNiX)_3O_4$ were systematically studied.

2. Experimental section

2.1. Experimental procedures

The $(MnFeCoNiX)_3O_4$ (X = Zn, Cu, Cr) HEOs were synthesized by heat treatment of the precursors prepared by the chemical co-precipitation method. Firstly, different chlorides including $MnCl_2$, $CoCl_2{\cdot}6H_2O$, $FeCl_2{\cdot}4H_2O$, $NiCl_2{\cdot}6H_2O$, $ZnCl_2/CuCl_2{\cdot}2H_2O/CrCl_3{\cdot}6H_2O$ were weighed with a molar ratio of Mn: Co: Fe: Ni: Zn/Cu/Cr = 1:1:1:1:1, separately. Then all these chlorides were dissolved by deionized water to form a transparent solution. Next, a required amount of ammonium hydroxide was added into the solution drop by drop until pH = 10 to obtain three different kinds of HEOs precursors. After being cleaned by deionized water and dried under 70 °C, a typical heat treatment of the $(MnFeCoNiCu)_3O_4$ precursors was performed at different temperatures (400 °C, 500 °C, 600 °C, 700 °C, 800 °C and 900 °C) in air for 4 h with a heating rate of 5 °C/min to obtain the corresponding HEOs. Based on the heat treatment of $(MnFeCoNiCu)_3O_4$ precursors, the processing parameters for the remaining two samples were set to 800 °C.

2.2. Characterization

The phase composition of the as-prepared HEOs was analyzed by X-ray diffractometer (XRD, Rigaku Ultima IV) at a step of 2°/min using Cu-Kα radiation, with a 2θ range of 20°–80°. The morphology and elemental composition of $(MnFeCoNiX)_3O_4$ (X = Zn, Cu, Cr) HEOs were characterized by a JEOL JSM 7001 F scanning electron microscope (SEM) equipped with an energy-dispersive spectroscope (EDS, IncaX-Max 80 T). The X-ray photoemission spectroscopy (XPS, AXIS Supra) was utilized to study the elemental valence state of the HEOs. The XRD results were refined using GSAS-II software suite. The peak shapes were modeled by using pseudo-Voigt profile functions and 15 background coefficients were fitted using Chebyschev-1 functions.

Thermal stability of the HEOs precursor was characterized by thermalgravimetric analysis (TGA, STA-409PC) in nitrogen atmosphere at a heating rate of 20 °C/min to 1000 °C. The synthesized HEOs powders were pressed into cylinders with a diameter of 3 mm and a height of 3 mm, then placed in a melting point apparatus (LZ-3, Institute of Iron and Steel Metallurgy, Tohoku University) under 900 °C–1200 °C for 10 min and the side view of the samples was recorded.

Magnetic measurements were conducted by a Vibrating Sample Magnetometer (VSM-220, YP) at room temperature with a magnetic field of −20000~20000 Oe. Microwave absorbing properties were analyzed by an Agilent N5244A Vector Network Analyzer (VNA, R&S ZNA, Germany) in a frequency range of 2~18 GHz. The HEOs powders were mixed with paraffin at the mass ratio of 7 : 3 and then the as-formed mixtures were molded into toroidal samples (thickness is 2–2.5 mm, inner diameter is 3.04 mm and outer diameter is 7 mm).

3. Results and discussion

3.1. Structural and morphologic analysis

XRD patterns of $(MnFeCoNiCu)_3O_4$ HEO calcined at different temperature (400 °C–900 °C) are presented in Fig. 1. One clear diffraction peak is observed at about 30.3° when calcination temperature increases from 400 °C to 500 °C, corresponding to (220) plane of spinel phase. With the temperature increasing up to 800 °C, the characteristic peaks belonging to (111), (220), (311), (222), (400), (422), (511), (440) and (533) planes of $NiFe_2O_4$ are clearly distinguished, with increased intensity and decreased FWHM [11]. In order to further confirm the crystal structure of the obtained three HEOs, the Rietveld refinement was performed and the results are shown in Fig. 2. The observed range of lattice parameters compares well with the reported value of spinel-structural Fe_3O_4 with the space group Fd-3m (a = 8.3578 Å) and no impurities was detected at this temperature [38], indicating that the $(MnFeCoNiX)_3O_4$ HEO is well-crystallized with spinel structure. Particularly, $(MnFeCoNiCr)_3O_4$ shows the strongest peak intensity, indicating better crystallinity [39].

SEM micrographs of $(MnFeCoNiCu)_3O_4$ HEO calcined at 500 °C–900 °C for 4 h are presented in Fig. 3 to understand the impact of calcination temperature on the HEO microstructures. As shown in Fig. 3 (a and b), the morphology of the HEO samples calcined at 500 °C and 600 °C exhibits a porous structure with sparsely stacked particles. As the calcination temperature increases, large particles gradually evolve into densely packed nano-particles, as shown in Fig. 3(c and d). With the

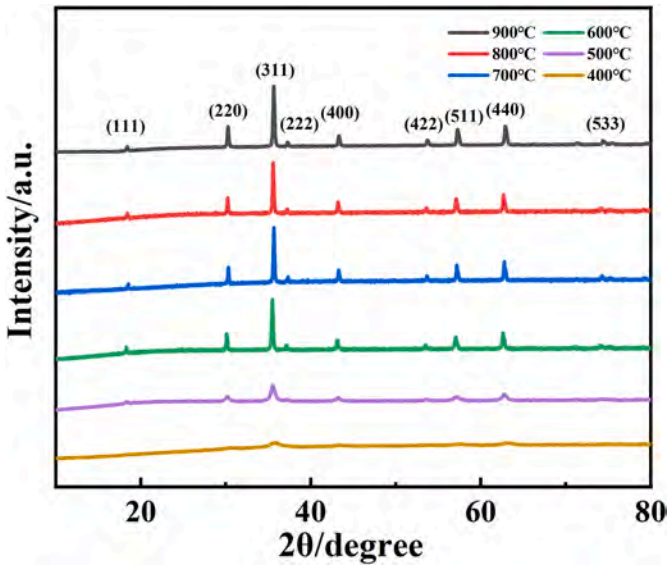

Fig. 1. XRD patterns of $(MnFeCoNiCu)_3O_4$ HEO calcined at different temperatures (400 °C–900 °C) for 4 h.

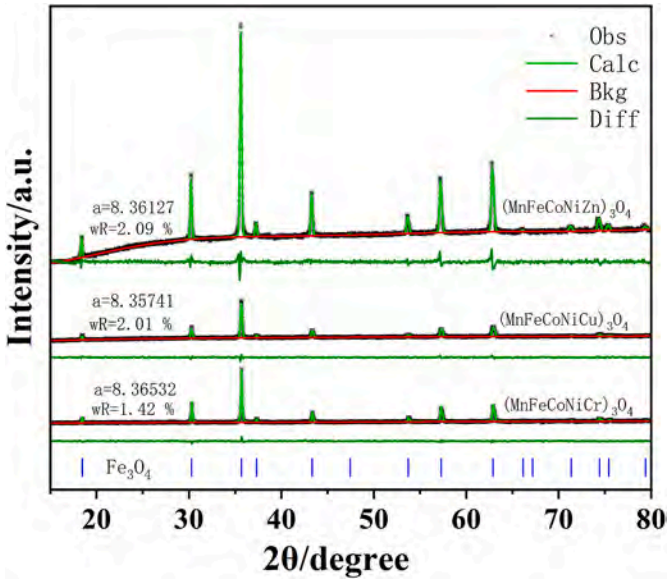

Fig. 2. Rietveld refinement of XRD patterns of $(MnFeCoNiX)_3O_4$ (X = Zn, Cu, Cr) HEOs calcined at 800 °C for 4 h.

temperature increasing to 900 °C, a large quantity of closely stacked grains was observed as a result of the aggregation and growth of nanoparticles. SEM images of different HEOs samples calcined at 800 °C for 4 h are displayed in Fig. 4. It can be seen that all the HEOs samples are composed of aggregated nano-particles. From Fig. 4(a and b), $(MnFeCoNiCu)_3O_4$ and $(MnFeCoNiZn)_3O_4$ exhibit a relatively smooth morphology, with the grain size ranging from 200–400 nm and 100–200 nm based on Fig. 4(d–e). As observed from Fig. 4(c), $(MnFeCoNiCr)_3O_4$ shows an irregularly porous architecture, with the grain size of 100~500 nm (Fig. 4(f)). Meanwhile, according to elemental mapping analysis of different HEOs samples shown in Fig. S(1–3), all the elements including Mn, Ni, Co, Fe and Cu/Zn/Cr are homogeneously distributed and no elemental segregation exists.

XPS spectra of $(MnFeCoNiCu)_3O_4$ were recorded to further study the chemical covalence and bonding. For the XPS spectrum of Mn 2p in Fig. 5(a), characteristic peaks at 641.1 eV (Mn $2p_{3/2}$) and 652.5 eV (Mn $2p_{1/2}$) indicate the presence of Mn^{2+}, while peaks at 642.7 eV (Mn $2p_{3/2}$) and 654.1 eV (Mn $2p_{1/2}$) demonstrate the existence of Mn^{3+} [40]. As shown in Fig. 5(b), the peaks at 854.7 eV and 871.5 eV are associated with Ni $2p_{3/2}$ and Ni $2p_{1/2}$ of Ni^{2+}, separately, and peaks at 855.7 eV and 873.1 eV are assigned to Ni $2p_{3/2}$ and Ni $2p_{1/2}$ of Ni^{3+}, separately [41]. For the Co 2p spectrum in Fig. 5(c), the peaks at 779.6 eV (Co $2p_{3/2}$) and 795.2 eV (Co $2p_{1/2}$) are connected with Co^{2+}, while peaks at 782.6 eV and 798.3 eV are related to Co^{3+} [42]. As for the Fe 2p spectrum shown in Fig. 5(d), peaks at 710.1 eV (Fe $2p_{3/2}$) and 722.7 eV (Fe $2p_{1/2}$) belong to Fe^{2+}, while 712.9 eV (Fe $2p_{3/2}$) and 724. 6eV (Fe $2p_{1/2}$) belong to Fe^{3+}.

The results reveal that the elements Mn, Co, Ni and Fe all exhibit +3 and + 2 valence states and thus they form a spinel structure, which is consistent with the XRD analysis.

It is worth mentioning that only Cu^{2+} was detected in the Cu 2p spectrum in Fig. 5(e), corresponding to two peaks at 933.4 eV (Cu $2p_{3/2}$) and 953.2 eV (Cu $2p_{1/2}$) [11]. Therefore, additional charge compensation becomes imperative within the lattice. According to Pauling's rule, in instances of positive charge excess, a material's inherent reaction to balance the surplus charge is to generate negative charge within the lattice [43,44]. The generation mechanism of charge generation in oxides involves the release of oxygen from the lattice, which is also confirmed by the XPS spectrum of O 1s. As shown in Fig. 5(f), the O 1s spectrum is deconvoluted into three subpeaks, where 529.9 eV corresponds to oxygen vacancy, 529.8 eV to lattice oxygen and 531.2 eV to surface-absorbed oxygen. Additionally, the increase in oxygen vacancies can heighten the diffusion of reactants to a certain extent while rendering additional electrons to acquire achievable capacity, which is favorable to facilitate conductivity [45].

3.2. Thermal stability

The thermal stability of the as-synthesized $(MnFeCoNiCu)_3O_4$ HEO precursor was investigated by thermogravimetric analysis (TGA) in N_2. As depicted in Fig. 6, the mass loss of the HEO sample mainly consists of four stages. The major weight loss (~15 wt%) happens at the first stage before 300 °C, which is mainly caused by the loss of the water molecules of hydration. At the second stage during 300 °C–500 °C, the weight loss (~10 wt%) should be ascribed to the decomposition of hydroxides. In the third stage in the temperature ranging from 500 °C to 750 °C, a slight weight loss of approximately 3 wt% was obtained, which is attributed to the gradual formation of the ferrite phase starting at 500 °C and the slow decay of the impurity phase, thereby resulting in a complete ferrite phase [46–48], which is in agreement with XRD results in Fig. 1. The mass change in the last stage after 750 °C is negligible, suggesting that spinel phase has completed. Fig. 7 shows the side view of $(MnFeCoNiCu)_3O_4$ HEO when heated at 900 °C–1200 °C. The results shows that the height of the HEO sample remains unchanged when temperature increases from 900 °C to 1000 °C. As the temperature continues to increase, the height and width of the sample slightly decrease at 1100 °C and keep stable at 1200 °C, indicating good high-temperature stability of $(MnFeCoNiCu)_3O_4$ HEO sample.

3.3. Magnetic properties

In order to investigate the extent to which different magnetic cations affect the magnetic properties of the materials, thus enabling a more in-depth analysis of the associated wave-absorbing properties, an exhaustive characterization of the magnetic properties has been carried out. The magnetic properties of $(MnFeCoNiX)_3O_4$ (X = Zn, Cu, Cr) HEOs are studied by hysteresis loops recorded at room temperature with an applied magnetic field ranging from −20000 to 20000 Oe, as illustrated in Fig. 8. Fig. 8(b) is the magnified hysteresis loops in the range of −600–600 Oe of Fig. 8(a). It can be clearly seen in Fig. 8(a) that the saturation magnetization (M_s) value, remanent magnetization (M_r) value and coercivity (H_c) value of $(MnFeCoNiZn)_3O_4$ are all approaching

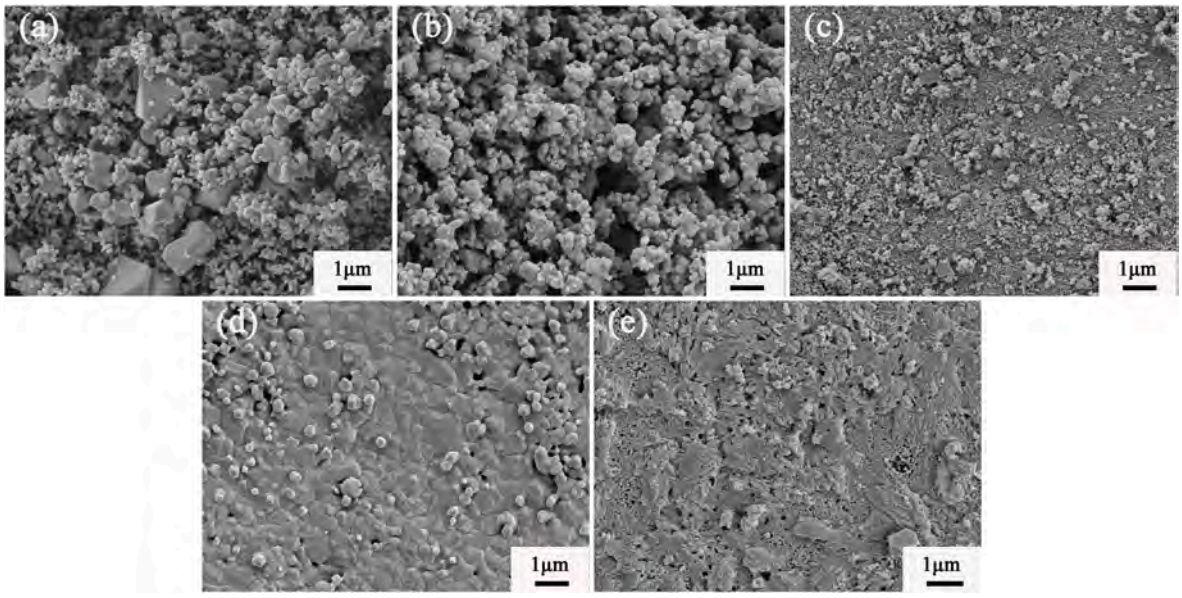

Fig. 3. SEM images of $(MnFeCoNiCu)_3O_4$ calcined at (a) 500 °C, (b) 600 °C, (c) 700 °C, (d) 800 °C, (e) 900 °C for 4 h.

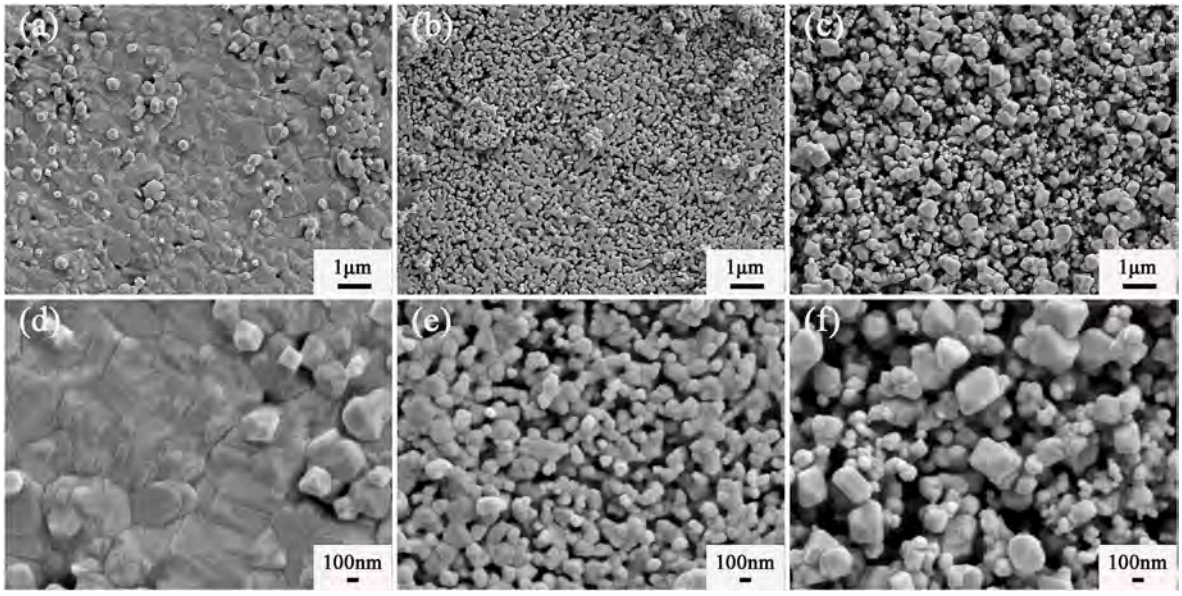

Fig. 4. SEM images of $(MnFeCoNiX)_3O_4$ HEO powder calcined at 800 °C for 4 h: ((a), (d)) $(MnFeCoNiCu)_3O_4$; ((b), (e)) $(MnFeCoNiZn)_3O_4$; ((c), (f)) $(MnFeCoNiCr)_3O_4$.

to zero, indicating that $(MnFeCoNiZn)_3O_4$ is a compound with substandard magnetic properties.

Comparing with another two samples, the inferior magnetic properties of $(MnFeCoNiZn)_3O_4$ are owning to the substitution of non-magnetic Zn^{2+} ions for magnetic Cr ions (2–3 μB) or Cu ions (3/2 μB), which will result in a dilution of the tetrahedral (A) and octahedral (B) sites, attenuating the exchange and declining the vector sum of lattice magnetic moments, in accordance with Neel's two-sublattice collinear model [36,49,50]. Meanwhile, the dramatic increase in crystal boundaries brought about by the decrease in crystallite size also contributes to the reduction in magnetic properties [51,52]. Moreover, $(MnFeCoNiCu)_3O_4$ HEO has the larger saturation magnetization (M_s) value of 38.6 emu/g compared with 19.7 emu/g of $(MnFeCoNiCr)_3O_4$, since the porosity of $(MnFeCoNiCr)_3O_4$ in Fig. 4 is significantly greater than that of $(MnFeCoNiCu)_3O_4$, which will disrupt the magnetic circuit between the grains and result in a net decrease in the magnetic properties [46]. Additionally, Fig. 8(b) also illustrates that the M_r values of $(MnFeCoNiCu)_3O_4$ and $(MnFeCoNiCr)_3O_4$ are 7.9 emu/g and 6.7 emu/g, which is in good consistence with the manner of M_s.

The coercivity is mainly related to the crystallinity, grain size, micro strain, porosity, lattice distortion, and anisotropy constant of the material. In general, the H_c of the same ferrite material is positively correlated with the Ms value. $(MnFeCoNiCu)_3O_4$ with a larger Ms value has the same coercivity (52.6 Oe) as $(MnFeCoNiCr)_3O_4$, which is mainly attributed to the fact that the domain wall motion of single domains is more likely to lead to a decrease in H_c with decreasing crystal size than magnetization rotation in nano-magnetic materials [36,53]. The remanent magnetization (M_r/M_s) is between 0.204 and 0.340, less than 0.5, indicating the formation of single domains without domain walls inside the material, which also exactly proves this. A similar phenomenon appears in the literature of chromium substituted lithium ferrites [48, 54].

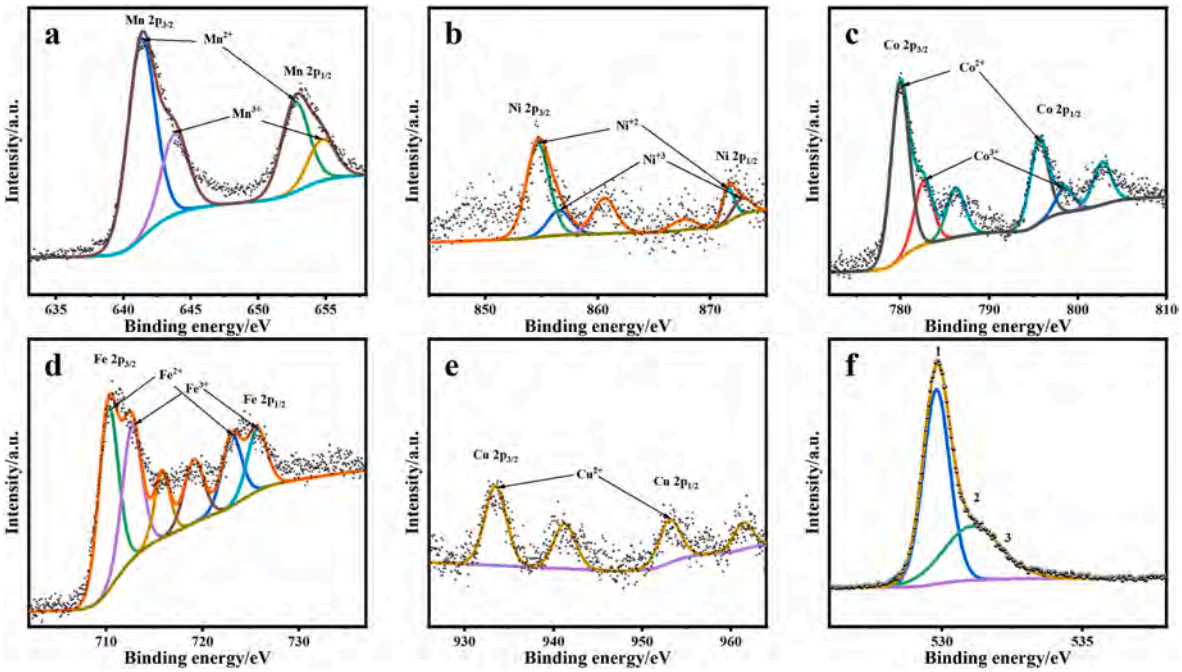

Fig. 5. XPS spectra of $(MnFeCoNiCu)_3O_4$: (a) Mn 2p; (b) Ni 2p; (c) Co 2p; (d) Fe 2p; (e) Cu 2p; (f) O 1s.

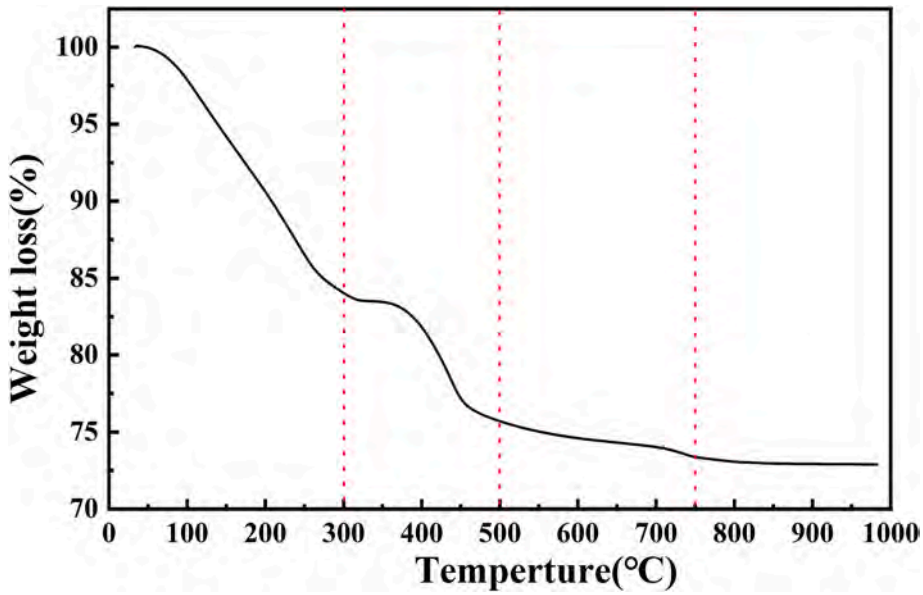

Fig. 6. TGA curve of $(MnFeCoNiCu)_3O_4$ HEO in N_2 atmosphere.

3.4. Electromagnetic wave-absorbing properties

To investigate the microwave absorbing properties of the synthesized $(MnFeCoNiX)_3O_4$ (X = Zn, Cu, Cr) HEOs, frequency dependencies of EM parameters of the samples are measured and depicted, as shown in Fig. 9. It is widely acknowledged that HEO's ability to store EM wave is represented by the real parts of permittivity (ε') and permeability (μ'), whereas the ability to dissipate EM energy is characterized by the imaginary parts of permittivity (ε'') and permeability (μ'') [55,56].

As illustrated in Fig. 9 (a – b), the real part of complex permittivity ε' decreases with increasing frequency and eventually stabilizes at high frequencies, showing obvious ferrimagnetic behavior and dispersion phenomena [57,58]. The frequency-dependent variation of the permittivity can be illustrated by the Koop theory and the Maxwell-Wagner double-layer model. In this model, the inhomogeneous dielectric structure is composed of insulating thinner grain boundaries and conductive grains separated by those boundaries. In an applied electromagnetic field, dipoles accumulate (space charge) at the resistive grain boundaries, resulting in polarization of the material and large ε' at low frequencies [59,60]. As the frequency increases, the dipole pairs are responsible for the polarization lag behind the electromagnetic field frequency to produce relaxation phenomena. Moreover, ferromagnetic resonance at high frequencies leads to the appearance of humps with a decreasing trend of the imaginary part of complex permittivity ε'' [32,33,57]. The largest value of ε'' for the $(MnFeCoNiCu)_3O_4$ sample is attributed to the fact that the introduced Cu enhances the ionic conductivity, implying better energy dissipation ability of the $(MnFeCoNiCu)_3O_4$ material. The permeability (μ' and μ'') represented in Fig. 9 (c - d) shows

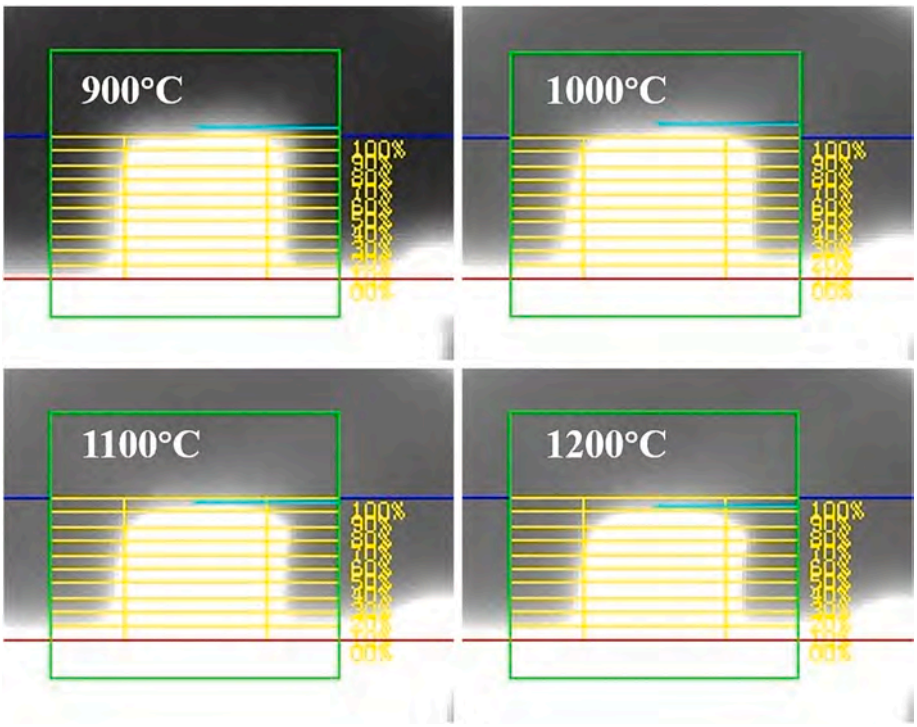

Fig. 7. Height changes of $(MnFeCoNiCu)_3O_4$ HEO at 900 °C–1200 °C.

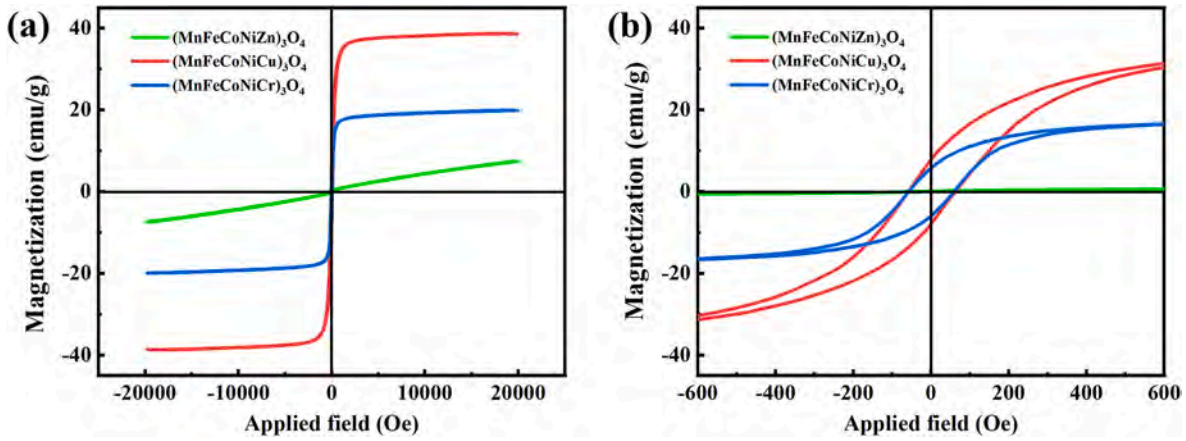

Fig. 8. Hysteresis loops of $(MnFeCoNiX)_3O_4$ (X = Zn, Cu, Cr): (a) −20000–20,000 Oe; (b) enlarged curve of −600–600 Oe.

similar trends, indicating the presence of natural resonance and natural exchange resonance in all samples. In general, the natural resonance is manifested by an oscillatory peak in the imaginary part of the permeability, at the same time, that the real part of the permeability decreases apparently [61,62]. From the Globus equation (1) [32],

$$\mu' \propto \left(M_s^2 D / K^{1/2}\right) \tag{1}$$

where D is the crystallize size, K typifies the magneto-crystalline anisotropy constant, and M_s represents the saturation magnetization, the highest value of M_s leads to the largest μ' of $(MnFeCoNiCu)_3O_4$ among the samples. Besides, the broad and strong resonance peaks of μ'' in the low-frequency range (8–9 GHz) are related to the natural resonance of ferrite [33,63]. According to the natural resonance equation (2) [64],

$$2\pi f_r = (4\gamma K) / (3\mu_0 M_s) \tag{2}$$

where γ is gyromagnetic ratio (≈2.8 GHz/kOe for ferrites), the higher M_s values shifted the resonance peaks of the $(MnFeCoNiCu)_3O_4$ samples slightly towards the low-frequency region. Furthermore, the anomalous increase of dynamic magnetic loss in the high-frequency region (14–18 GHz) for all samples is probably related to eddy current losses. A similar phenomenon occurs in ferrite materials with similar compositions [33].

Commonly, the magnetic tangent loss (μ''/μ') and dielectric tangent loss ($\varepsilon''/\varepsilon'$) are the two main reference indexes to symbolize the EM wave attenuation ability. As shown in Fig. 9 (e – f), μ''/μ' and $\varepsilon''/\varepsilon'$ values of $(MnFeCoNiCu)_3O_4$ are larger than the other two samples, which is in accord with the as-mentioned results from Fig. 9 (a – d). Interestingly, the dielectric tangent loss ($\varepsilon''/\varepsilon'$) shows obvious downtrend while the magnetic tangent loss (μ''/μ') exhibits rapid uptrend at higher frequencies. The complementary trend of magnetic and dielectric loss can make it possible for the $(MnFeCoNiX)_3O_4$ HEOs in this work to achieve whole-band wave adsorption.

As an important index of evaluating the comprehensive EM wave attenuation ability of materials, attenuation constant (α) is defined by Eq. (3) [65]:

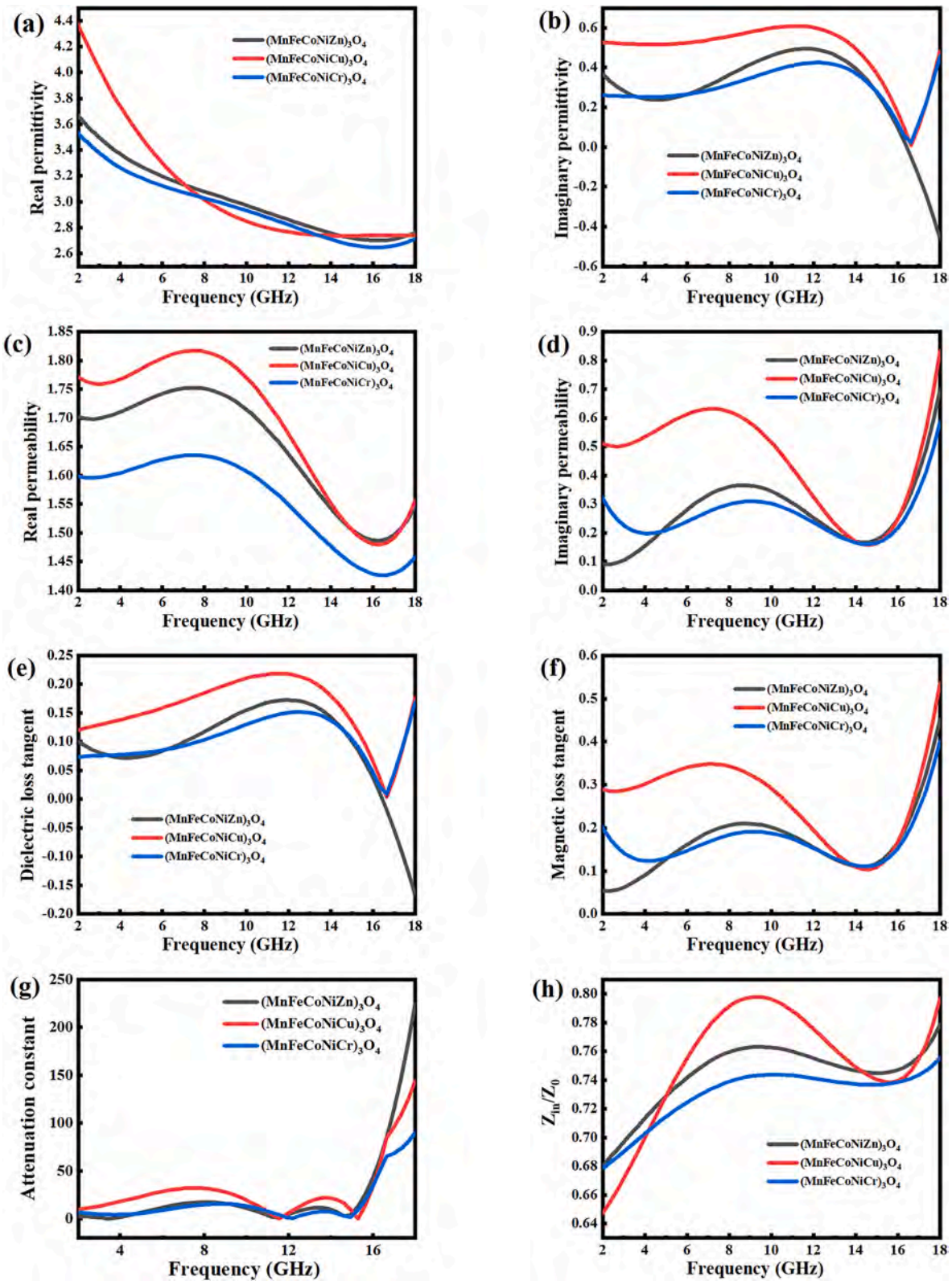

Fig. 9. EM parameters of $(MnFeCoNiX)_3O_4$ (X = Zn, Cu, Cr) HEOs: (a) real part of permittivity (ε′); (b) imaginary part of permittivity (ε″); (c) real part of permeability (μ′); (d) imaginary part of permeability (μ″); (e) dielectric tangent loss (ε″/ε′); (f) magnetic tangent loss (μ″/μ′); (g) attenuation constant (α) and (h) impedance match (Z_{in}/Z_0).

$$\alpha = \frac{\sqrt{2}\pi f}{c}\sqrt{\left(\mu''\varepsilon'' - \mu'\varepsilon'\right) + \sqrt{\left(\mu''\varepsilon'' - \mu'\varepsilon'\right)^2 + \left(\mu'\varepsilon'' + \mu''\varepsilon'\right)^2}} \quad (3)$$

where f is the EM wave frequency; c represents the light velocity (3×10^8 m/s); μ′ and μ″ symbolize the real and imaginary parts of permeability, respectively; ε′ and ε″ are the real and imaginary parts of permittivity. As depicted in Fig. 9(g), the attenuation constant peaks

arising at 8 GHz and 14 GHz indicate that the magnetic loss accounts for natural resonance and the dielectric loss contributes to the variation of loss capability at this frequency, respectively. Obviously, $(MnFeCoNiCu)_3O_4$ exhibits relatively better broadband adsorption ability since it has the largest α value at almost the whole band among the three samples.

The impedance matching performance is often used to evaluate the ease with which EM microwaves penetrate the absorber materials. Basically, the value of impedance matching (Z) is defined by Eq. (4):

$$Z = Z_{in}/Z_0 \tag{4}$$

where Z_{in} is input impedance of absorber and Z_0 is the impedance of free space. And the correlation of Z_{in} and Z_0 can be found in Eq. (5) [66]:

$$Z_{in} = Z_0 \sqrt{\frac{\mu_r}{\varepsilon_r}} \tanh\left(j\frac{2\pi f d\sqrt{\mu_r \varepsilon_r}}{c}\right) \tag{5}$$

where μ_r and ε_r are relative complex permeability and relative complex permittivity, separately; d stands for the sample thickness. Generally, Z_{in} being closer to Z_0 is more beneficial for EM microwaves entering into the absorbers. As shown in Fig. 9 (h), the calculated impedance matching value of $(MnFeCoNiCu)_3O_4$ specimen is much closer to 1 than those of $(MnFeCoNiZn)_3O_4$ and $(MnFeCoNiCr)_3O_4$, which makes the $(MnFeCoNiCu)_3O_4$ HEO as a promising EM microwave absorber candidate.

Reflection loss (RL), which is determined by Eq. (6) [67], is widely viewed as an essential index to evaluate the EM wave-absorbing performance.

$$RL\ (dB) = 20\lg\left|\frac{Z_{in} - Z_0}{Z_{in} + Z_0}\right| \tag{6}$$

Normally, materials with a RL value less than −10 dB can be seen as the effective EM wave-absorbers and the corresponding frequency range when RL < −10 dB is called the effective absorption bandwidth (EAB) [68]. Fig. 10 exhibits the RL trend in 2–18 GHz frequency range of $(MnFeCoNiCu)_3O_4$ samples calcined at 500 °C–900 °C with different sample thickness (1–5 mm). The RL_{min} values of the samples calcined at 600 °C and 700 °C are comparable, varying from −10.1 dB to −10.6 dB. Notably, the RL_{min} value enhances to −15.5 dB as the calcination temperature rises to 800 °C and deteriorates to −11.7 dB at 900 °C. Therefore, the $(MnFeCoNiCu)_3O_4$ HEO can be endowed with the best EM microwave absorbing properties with a calcination temperature of 800 °C.

The RL values of different $(MnFeCoNiX)_3O_4$ (X = Zn, Cu, Cr) HEOs with different sample thicknesses (1–5 mm) calcined at 800 °C are presented in Fig. 11. Fig. 11 (a) shows that the RL_{min} value of $(MnFeCoNiZn)_3O_4$ can reach −11.3 dB and a relatively wide effective absorption bandwidth (EAB) can be achieved by adjusting the thickness (3.0–5.0 mm) of the absorber in the frequency range of 8.14–12.9 GHz. Compared with $(MnFeCoNiZn)_3O_4$, $(MnFeCoNiCu)_3O_4$ is able to achieve a smaller RL_{min} value (−15.5 dB) and a much wider EAB can be realized by adjusting the sample thickness (2.5–5.0 mm) in the frequency range of 4.4–13.92 GHz, as shown in Fig. 11 (b). However, the RL_{min} value of $(MnFeCoNiCr)_3O_4$ is only −10.2 dB, as shown in Fig. 11 (c). Fig. 11 (d ~ f) illustrates the 3D presentations of the RL curves of the three samples. It can be observed in Fig. 11(d) and (f) that the EAB of $(MnFeCoNiZn)_3O_4$ and $(MnFeCoNiCr)_3O_4$ are 4.08 GHz and 1.7 GHz when the sample thickness is 4 mm, respectively. By comparison, $(MnFeCoNiCu)_3O_4$ possesses a wider EAB of 8.84 GHz with the sample thickness of 5 mm, suggesting that $(MnFeCoNiCu)_3O_4$ sample exhibits the best microwave absorbing properties. As aforementioned, $(MnFeCoNiCu)_3O_4$ specimen exhibits the smallest lattice parameter, more dense morphology and higher Ms value, which leads to higher permittivity and permeability to effectively store and dissipate electromagnetic waves. Therefore. $(MnFeCoNiCu)_3O_4$ sample shows the best electromagnetic wave absorption properties among the three specimens.

Fig. 12 summarizes the thickness versus EAB of the single-phase spinel HEOs synthesized in this work, as well as oxide-based [69–71], ferrite-based [33,72–74], transition metal carbide-based [75], and transition metal boride-based [76,77] materials. Although the RL values of the obtained HEOs are not prominent enough, it is noteworthy that the HEOs have a sufficiently wide EAB, thus make them a promising wave-absorbing material.

4. Conclusion

In conclusion, three kinds of $(MnFeCoNiX)_3O_4$ (X = Zn, Cu, Cr) HEOs materials are fabricated via chemical co-precipitation and solid-reaction method. XRD results show that single-phase spinel structure with Fd-3m

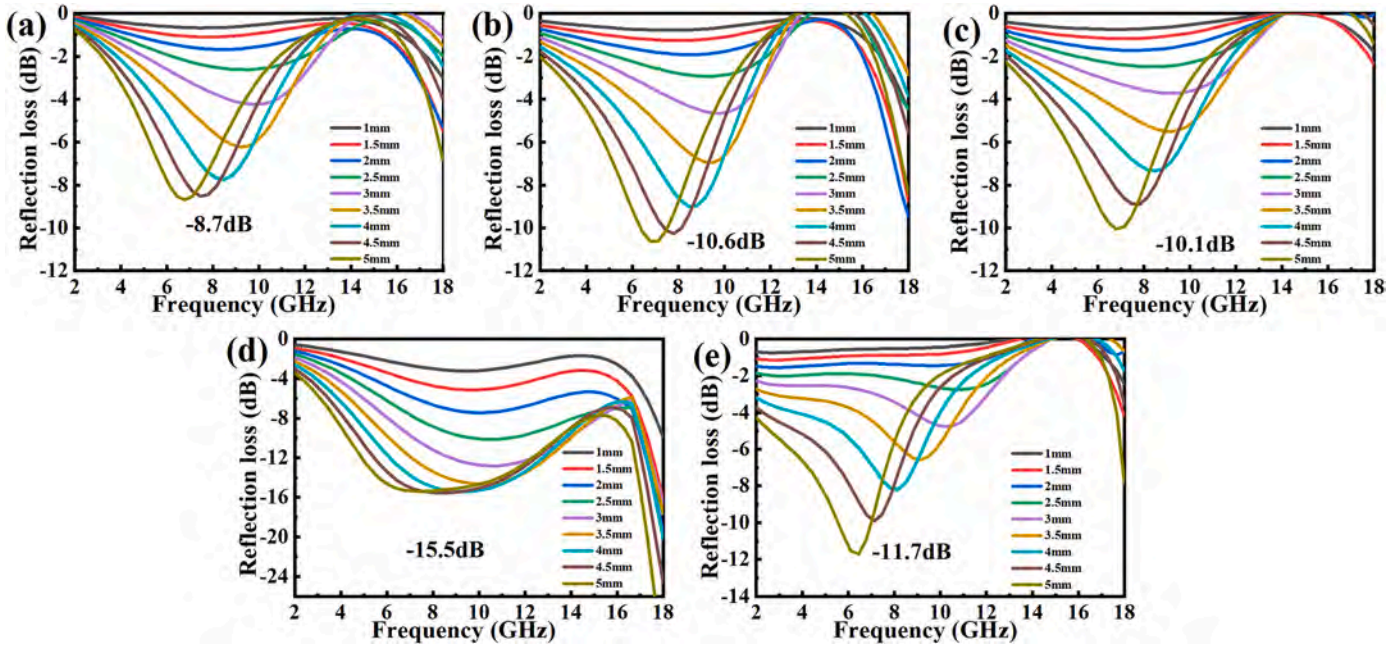

Fig. 10. Frequency dependencies (2–18 GHz) of reflection loss (RL) for $(MnFeCoNiCu)_3O_4$ calcined at (a) 500 °C, (b) 600 °C, (c) 700 °C, (d) 800 °C and (e) 900 °C for 4 h with different sample thicknesses (1–5 mm).

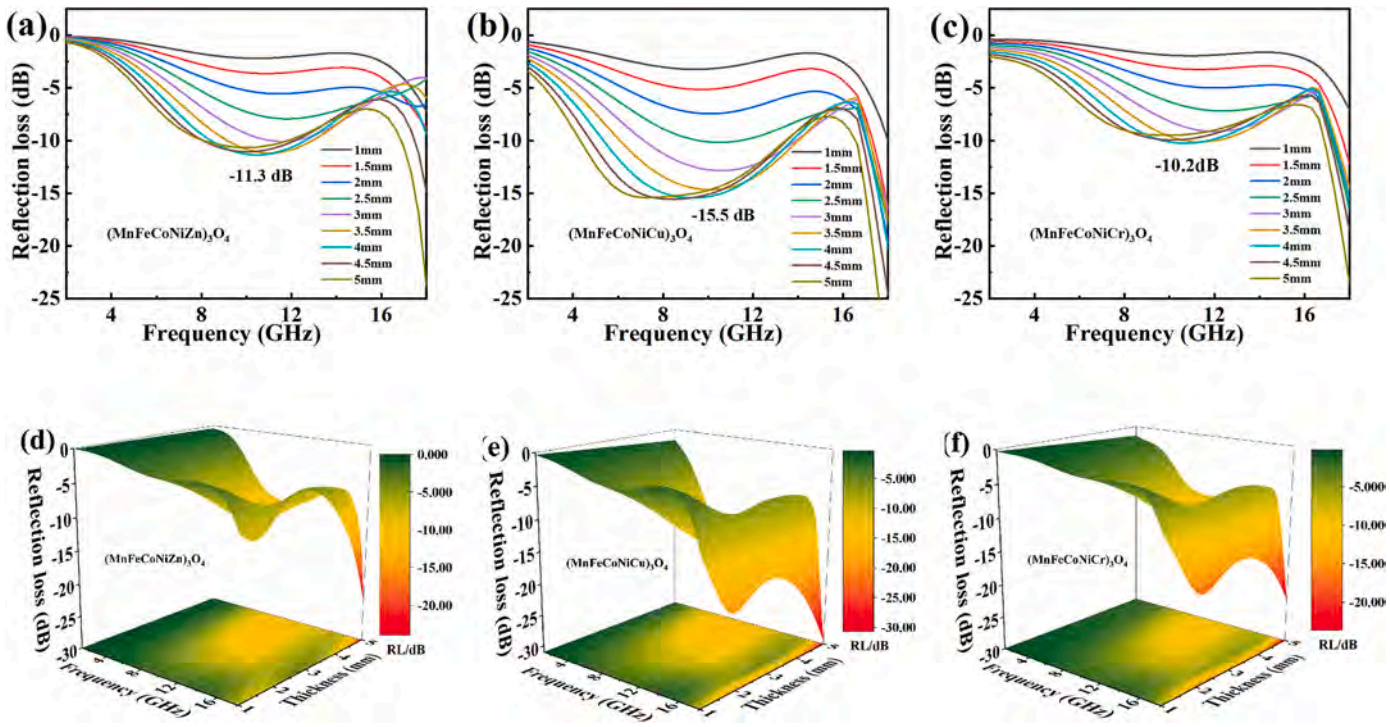

Fig. 11. Frequency dependences (2–18 GHz) of reflection loss (RL) for $(MnFeCoNiX)_3O_4$ (X = Zn, Cu, Cr) HEOs with different sample thicknesses (1–5 mm) after calcined at 800 °C for 4 h: (a–c) 2D curves and (d–f) 3D presentations.

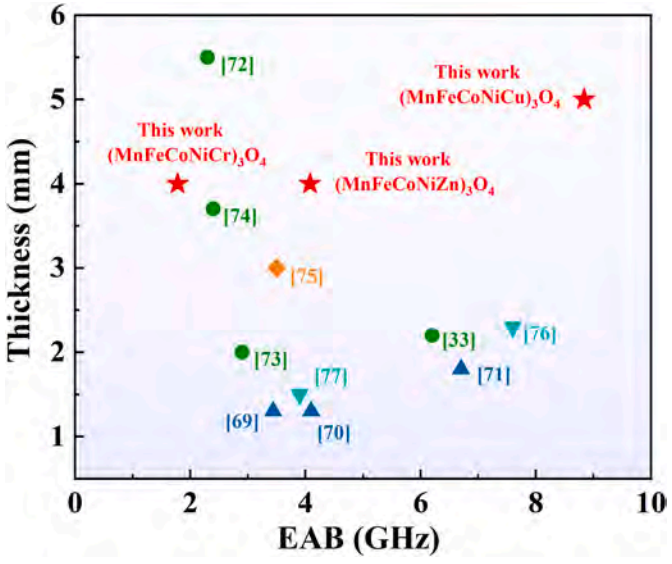

Fig. 12. EAB and the corresponding thickness of $(MnFeCoNiX)_3O_4$ (X = Zn, Cu, Cr) samples and various kinds of reported EM absorbing materials: MnO_2 [69], ZnO_2 [70], CrO_2/Cr_2O_3 [71], Fe_3O_4 [72], $NiFe_2O_4$ [73], $(MnNiCuZn)_{0.7}Co_{0.3}Fe_2O_4$ [74], (Zr,Hf,Nb,Ta)C [75], $(Zr_{0.25}Hf_{0.25}Nb_{0.25}Ta_{0.25})B_2$ [76], (Ce,Y,Sm,Er,Yb)B_6 [77].

space group is obtained after the samples are calcined at above 800 °C. The grain size of the HEOs samples ranges from 100 nm to 500 nm, with a uniform elemental distribution based on SEM analysis. Furthermore, XPS results confirm that Mn, Ni, Co and Fe are all in +2 and + 3 state and Cu is in +2 state. Compared with $(MnFeCoNiZn)_3O_4$ and $(MnFeCoNiCr)_3O_4$, $(MnFeCoNiCu)_3O_4$ sample shows the best magnetic properties with a remanent magnetization (M_r) value of 7.9 emu/g, a saturation magnetization (M_s) value of 38.6 emu/g and a coercivity (H_c) of 52.6 Oe. On the other hand, $(MnFeCoNiCu)_3O_4$ HEO sample calcined at 800 °C displays the best EM microwave absorbing performance due to the largest attenuation constant (α) at almost the whole band and the largest impedance matching (Z) value close to 1. Meanwhile, the $(MnFeCoNiCu)_3O_4$ sample is able to achieve a minimum reflection loss (RL) of −15.5 dB and presents the widest EAB of 8.84 GHz with the thickness of 5 mm. Also, the as-synthesized $(MnFeCoNiCu)_3O_4$ sample exhibits excellent high-temperature resistance above 900 °C, making it a promisingly powerful wide-band EM microwave absorber in harsh environment.

Declaration of competing interest

The authors declare that they have no known competing financial interests or personal relationships that could have appeared to influence the work reported in this paper.

Acknowledgements

This work was supported by the National Natural Science Foundation of China (No. U2004177), Henan Province Key Research Project for Higher Education Institutions (No. 23B430017), the Outstanding Youth Fund of Henan Province (No. 212300410081), and the Science and Technology Innovation Talents in Universities of Henan Province (CN) (No. 22HASTIT001). Bingbing Fan also acknowledged the financial support from the Research and Entrepreneurship Start-up Projects for Overseas Returned Talents. Wei Li is grateful to the financial support by the Technical University of Darmstadt.

Appendix A. Supplementary data

Supplementary data to this article can be found online at https://doi.org/10.1016/j.ceramint.2024.01.383.

References

[1] C.M. Rost, E. Sachet, T. Borman, A. Moballegh, E.C. Dickey, D. Hou, J.L. Jones, S. Curtarolo, J.-P. Maria, Entropy-stabilized oxides, Nat. Commun. 6 (2015) 8485, https://doi.org/10.1038/ncomms9485.

[2] M. Li, Q. Zhi, J. Li, C. Wu, X. Jiang, Z. Min, R. Zhang, H. Wang, H. Wang, B. Fan, Sr$(Cr_{0.2}Mn_{0.2}Fe_{0.2}Co_{0.2}Ni_{0.2})O_3$: a novel high-entropy perovskite oxide with enhanced electromagnetic wave absorption properties, J Materiomics (2023), https://doi.org/10.1016/j.ceramint.2023.03.290.

[3] J.X. Liu, L. Guo, Y. Wu, Y. Qin, Y. Liang, G.J. Zhang, Lattice rigidity in high-entropy carbide ceramics with carbon vacancies, J. Am. Ceram. Soc. (2023) 106, https://doi.org/10.1111/jace.19206.

[4] Z. Wen, Z. Tang, Y. Liu, L. Zhuang, H. Yu, Y. Chu, Ultrastrong and high thermal insulating porous high-entropy ceramics up to 2000 °C, Adv. Mater. (2024) 2311870, https://doi.org/10.1002/adma.202311870.

[5] Z. Tang, Z. Wen, Y. Liu, L. Zhuang, H. Yu, Y. Chu, Rapid experimental screening of high-entropy diborides for superior oxidation resistance, Adv. Funct. Mater. (2023) 2312239, https://doi.org/10.1002/adfm.202312239.

[6] Y. Qin, J.C. Wang, J.X. Liu, X.F. Wei, F. Li, G.J. Zhang, C. Jing, J. Zhao, H. Wu, High-entropy silicide ceramics developed from (TiZrNbMoW)Si_2 formulation doped with aluminum, J. Eur. Ceram. Soc. 40 (2020) 2752–2759, https://doi.org/10.1016/j.jeurceramsoc.2020.02.059.

[7] R.R. Shahi, A.K. Gupta, P. Kumari, Perspectives of high entropy alloys as hydrogen storage materials, Int. J. Hydrogen Energy 48 (2023) 21412–21428, https://doi.org/10.1038/srep36770.

[8] M.-H. Tsai, J.-W. Yeh, High-entropy alloys: a critical review, Mater. Res. Lett. 2 (2014) 107–123, https://doi.org/10.1080/21663831.2014.912690.

[9] A. Sarkar, B. Breitung, H. Hahn, High entropy oxides: the role of entropy, enthalpy and synergy, Scripta Mater. 187 (2020) 43–48, https://doi.org/10.1016/j.scriptamat.2020.05.019.

[10] Y. Wang, J. Mi, Z.-S. Wu, Recent status and challenging perspective of high entropy oxides for chemical catalysis, Chem Catal. 2 (2022) 1624–1656, https://doi.org/10.1016/j.checat.2022.05.003.

[11] Y. Wang, H. Li, H. Liu, L. Yang, C. Zeng, Preparation and formation mechanism of Cr-free spinel-structured high entropy oxide $(MnFeCoNiCu)_3O_4$, Ceram. Int. 49 (2023) 1940–1946, https://doi.org/10.1016/j.ceramint.2022.09.159.

[12] Y.Y. Cheng, L. Zhou, J.X. Liu, Y.F. Tan, G.J. Zhang, Grain growth inhibition by sluggish diffusion and Zener pinning in high-entropy diboride ceramics, J. Am. Ceram. Soc. 106 (2023) 4997–5004, https://doi.org/10.1111/jace.19128.

[13] P. Kumari, A.K. Gupta, R.K. Mishra, M. Ahmad, R.R. Shahi, A comprehensive review: recent progress on magnetic high entropy alloys and oxides, J. Magn. Magn Mater. 554 (2022) 169142, https://doi.org/10.1016/j.jmmm.2022.169142.

[14] M. Lim, Z. Rak, J. Braun, C. Rost, G. Kotsonis, P. Hopkins, J.-P. Maria, D. Brenner, Influence of mass and charge disorder on the phonon thermal conductivity of entropy stabilized oxides determined by molecular dynamics simulations, J. Appl. Phys. 125 (2019), https://doi.org/10.1063/1.5080419.

[15] R. Djenadic, A. Sarkar, O. Clemens, C. Loho, M. Botros, V.S. Chakravadhanula, C. Kübel, S.S. Bhattacharya, A.S. Gandhi, H. Hahn, Multicomponent equiatomic rare earth oxides, Mater. Res. Lett. 5 (2017) 102–109, https://doi.org/10.1080/21663831.2016.1220433.

[16] Y. Han, R. Yu, H. Liu, Y. Chu, Synthesis of the superfine high-entropy zirconate nanopowders by polymerized complex method, J. Adv. Ceram. 11 (2022) 136–144, https://doi.org/10.1007/s40145-021-0522-x.

[17] S. Jiang, T. Hu, J. Gild, N. Zhou, J. Nie, M. Qin, T. Harrington, K. Vecchio, J. Luo, A new class of high-entropy perovskite oxides, Scripta Mater. 142 (2018) 116–120, https://doi.org/10.1016/j.scriptamat.2017.08.040.

[18] Wei Peng, Lei Zhuang, Hulei Yu, Yexia Qin, Y. Chu, Low-temperature molten salt synthesis of ultrafine high-entropy rare-earth silicate powders, J. Am. Ceram. Soc. 107 (2024) 1372–1382, https://doi.org/10.1111/jace.19512.

[19] Hong Meng, Wei Peng, Zhongyu Tang, Hulei Yu, Y. Chu, Data-driven discovery of formation ability descriptors for high-entropy rare-earth monosilicates, J Materiomics (2023), https://doi.org/10.1016/j.jmat.2023.11.017.

[20] M. Stygar, J. Dąbrowa, M. Moździerz, M. Zajusz, W. Skubida, K. Mroczka, K. Berent, K. Świerczek, M. Danielewski, Formation and properties of high entropy oxides in Co-Cr-Fe-Mg-Mn-Ni-O system: novel (Cr, Fe,Mg, Mn, Ni)$_3O_4$ and (Co, Cr, Fe, Mg, Mn)$_3O_4$ high entropy spinels, J. Eur. Ceram. Soc. 40 (2020) 1644–1650, https://doi.org/10.1016/j.jeurceramsoc.2019.11.030.

[21] X. Xie, B. Wang, Y. Wang, C. Ni, X. Sun, W. Du, Spinel structured MFe_2O_4 (M= Fe, Co, Ni, Mn, Zn) and their composites for microwave absorption: a review, Chem. Eng. J. 428 (2022) 131160, https://doi.org/10.1016/j.cej.2021.131160.

[22] J. Xue, H. Zhang, J. Zhao, X. Ou, Y. Ling, Characterization and microwave absorption of spinel MFe_2O_4 (M= Mg, Mn, Zn) nanoparticles prepared by a facile oxidation-precipitation process, J. Magn. Magn Mater. 514 (2020) 167168, https://doi.org/10.1016/j.jmmm.2020.167168.

[23] Y. Shen, Y. Wei, J. Ma, Y. Zhang, B. Ji, J. Tang, L. Zhang, P. Yan, X. Du, Self-cleaning functionalized FeNi/$NiFe_2O_4$/NiO/C nanofibers with enhanced microwave absorption performance, Ceram. Int. 46 (2020) 13397–13406, https://doi.org/10.1016/j.ceramint.2020.02.121.

[24] Y. Wang, Y. Fu, X. Wu, W. Zhang, Q. Wang, J. Li, Synthesis of hierarchical core-shell $NiFe_2O_4$@MnO_2 composite microspheres decorated graphene nanosheet for enhanced microwave absorption performance, Ceram. Int. 43 (2017) 11367–11375, https://doi.org/10.1016/j.ceramint.2017.05.344.

[25] K. Zhang, X. Gao, Q. Zhang, H. Chen, X. Chen, Fe_3O_4 nanoparticles decorated MWCNTs@C ferrite nanocomposites and their enhanced microwave absorption properties, J. Magn. Magn Mater. 452 (2018) 55–63, https://doi.org/10.1016/j.jmmm.2017.12.039.

[26] V. Dutta, S. Sharma, P. Raizada, A. Hosseini-Bandegharaei, V.K. Gupta, P. Singh, Review on augmentation in photocatalytic activity of $CoFe_2O_4$ via heterojunction formation for photocatalysis of organic pollutants in water, J. Saudi Chem. Soc. 23 (2019) 1119–1136, https://doi.org/10.1016/j.jscs.2019.07.003.

[27] K. Malaie, M.R. Ganjali, Spinel nano-ferrites for aqueous supercapacitors; linking abundant resources and low-cost processes for sustainable energy storage, J. Energy Storage 33 (2021) 102097, https://doi.org/10.1016/j.est.2020.102097.

[28] L. Sun, L. Zhan, Y. Shi, L. Chu, G. Ge, Z. He, Microemulsion synthesis and electromagnetic wave absorption properties of monodispersed Fe_3O_4/polyaniline core–shell nanocomposites, Synthetic Met 187 (2014) 102–107, https://doi.org/10.1016/j.synthmet.2013.11.007.

[29] K. Ali, J. Iqbal, T. Jan, I. Ahmad, D. Wan, A. Bahadur, S. Iqbal, Synthesis of $CuFe_2O_4$-ZnO nanocomposites with enhanced electromagnetic wave absorption properties, J. Alloys Compd. 705 (2017) 559–565, https://doi.org/10.1016/j.jallcom.2017.01.264.

[30] H. Lv, X. Liang, Y. Cheng, H. Zhang, D. Tang, B. Zhang, G. Ji, Y. Du, Coin-like α-Fe_2O_3@$CoFe_2O_4$ core–shell composites with excellent electromagnetic absorption performance, ACS Appl. Mater. Interfaces 7 (2015) 4744–4750, https://doi.org/10.1021/am508438s.

[31] A. Radoń, Ł. Hawełek, D. Łukowiec, J. Kubacki, P. Włodarczyk, Dielectric and electromagnetic interference shielding properties of high entropy (Zn, Fe, Ni, Mg, Cd)Fe_2O_4 ferrite, Sci. Rep. 9 (2019) 20078, https://doi.org/10.1038/s41598-019-56586-6.

[32] D. Mandal, K. Mandal, Electromagnetic wave attenuation properties of MFe_2O_4 (M= Mn, Fe, Co, Ni, Cu, Zn) nano-hollow spheres in search of an efficient microwave absorber, J. Magn. Magn Mater. 536 (2021) 168127, https://doi.org/10.1016/j.jmmm.2021.168127.

[33] J. Ma, B. Zhao, H. Xiang, F.-Z. Dai, Y. Liu, R. Zhang, Y. Zhou, High-entropy spinel ferrites MFe_2O_4 (M= Mg, Mn, Fe, Co, Ni, Cu, Zn) with tunable electromagnetic properties and strong microwave absorption, J. Adv. Ceram. 11 (2022) 754–768, https://doi.org/10.1007/s40145-022-0569-3.

[34] J. Dąbrowa, M. Stygar, A. Mikuła, A. Knapik, K. Mroczka, W. Tejchman, M. Danielewski, M. Martin, Synthesis and microstructure of the (Co, Cr, Fe, Mn, Ni)$_3O_4$ high entropy oxide characterized by spinel structure, Mater. Lett. 216 (2018) 32–36, https://doi.org/10.1016/j.matlet.2017.12.148.

[35] A. Mao, H.-Z. Xiang, Z.-G. Zhang, K. Kuramoto, H. Zhang, Y. Jia, A new class of spinel high-entropy oxides with controllable magnetic properties, J. Magn. Magn Mater. 497 (2020) 165884, https://doi.org/10.1016/j.jmmm.2019.165884.

[36] S. Dai, M. Li, X. Wang, H. Zhu, Y. Zhao, Z. Wu, Fabrication and magnetic property of novel (Co, Zn, Fe, Mn, Ni)$_3O_4$ high-entropy spinel oxide, J. Magn. Magn Mater. 536 (2021) 168123, https://doi.org/10.1016/j.jmmm.2021.168123.

[37] B. Musicó, Q. Wright, T.Z. Ward, A. Grutter, E. Arenholz, D. Gilbert, D. Mandrus, V. Keppens, Tunable magnetic ordering through cation selection in entropic spinel oxides, Phys. Rev. Lett. 3 (2019) 104416, https://doi.org/10.1103/PhysRevMaterials.3.104416.

[38] L.W. Finger, R.M. Hazen, A.M. Hofmeister, High-Pressure crystal chemistry of spinel ($MgAl_2O_4$) and magnetite (Fe_3O_4): Comparisons with silicate spinels, Phys. Chem. Miner. 13 (1986) 215–220, https://doi.org/10.1007/BF00308271.

[39] A. Esmaeilzaei, J.V. Khaki, S. abdolkarim Sajjadi, S. Mollazadeh, Synthesis and crystallization of (Co, Cr, Fe, Mn, Ni)$_3O_4$ high entropy oxide: the role of fuel and fuel-to-oxidizer ratio, J. Solid State Chem. 321 (2023) 123912, https://doi.org/10.1016/j.jssc.2023.123912.

[40] J. Wang, D. Stenzel, R. Azmi, S. Najib, K. Wang, J. Jeong, A. Sarkar, Q. Wang, P. A. Sukkurji, T. Bergfeldt, Spinel to rock-salt transformation in high entropy oxides with Li incorporation, Electrochemistry 1 (2020) 60–74, https://doi.org/10.3390/electrochem1010007.

[41] D. Wang, S. Jiang, C. Duan, J. Mao, Y. Dong, K. Dong, Z. Wang, S. Luo, Y. Liu, X. Qi, Spinel-structured high entropy oxide $(FeCoNiCrMn)_3O_4$ as anode towards superior lithium storage performance, J. Alloys Compd. 844 (2020) 156158, https://doi.org/10.1016/j.jallcom.2020.156158.

[42] W. Yiliang, A. Yunlong, Y. Shuwei, L. Bingliang, Z. Zhenhuan, O. Sheng, H. Wen, C. Weihua, L. Changhong, Z. Jianjun, Facile synthesis and supercapacitor performance of M_3O_4 (M= FeCoCrMnMg) high entropy oxide powders, J. Inorg. Mater. 36 (2021) 425–430, https://doi.org/10.15541/jim20200388.

[43] T.K. Andersen, D.D. Fong, L.D. Marks, Pauling's rules for oxide surfaces, Surf. Sci. Rep. 73 (2018) 213–232, https://doi.org/10.1016/j.surfrep.2018.08.001.

[44] G.V. Gibbs, F.C. Hawthorne, G.E. Brown Jr., Pauling's rules for oxide-based minerals: a re-examination based on quantum mechanical constraints and modern applications of bond-valence theory to Earth materials, Am. Mineral. 107 (2022) 1219–1248, https://doi.org/10.2138/am-2021-7938.

[45] M. Liao, J. Wang, L. Ye, H. Sun, Y. Wen, C. Wang, X. Sun, B. Wang, H. Peng, Extraction of oxygen anions from vanadium oxide making deeply cyclable aqueous zinc ion battery, Angew. Chem. Ed. Int 59 (2019) 2273–2278, https://doi.org/10.1002/anie.201912203.

[46] P. Hankare, V. Vader, N. Patil, S. Jadhav, U. Sankpal, M. Kadam, B. Chougule, N. Gajbhiye, Synthesis, characterization and studies on magnetic and electrical properties of Mg ferrite with Cr substitution, Mater. Chem. Phys. 113 (2009) 233–238, https://doi.org/10.1016/j.matchemphys.2008.07.066.

[47] M.A. Khan, M. Sabir, A. Mahmood, M. Asghar, K. Mahmood, M.A. Khan, I. Ahmad, M. Sher, M.F. Warsi, High frequency dielectric response and magnetic studies of $Zn_{1-x}Tb_xFe_2O_4$ nanocrystalline ferrites synthesized via micro-emulsion technique, J. Magn. Magn Mater. 360 (2014) 188–192, https://doi.org/10.1016/j.jmmm.2014.02.059.

[48] S.Y. Mulushoa, C.V. Kumari, V. Raghavendra, K.E. Babu, B. Murthy, K. Suribabu, Y. Ramakrishna, N. Murali, Effect of Zn–Cr substitution on the structural, magnetic

and electrical properties of magnesium ferrite materials, Phys. B Condens. Matter 572 (2019) 139–147, https://doi.org/10.1016/j.physb.2019.07.057.
[49] D. Kurmude, C. Kale, P. Aghav, D. Shengule, K. Jadhav, Superparamagnetic behavior of zinc-substituted nickel ferrite nanoparticles and its effect on mossbauer and magnetic parameters, J. Supercond. Nov. Magnetism 27 (2014) 1889–1897, https://doi.org/10.1007/s10948-014-2535-y.
[50] C. Zhen, X. Zhang, W. Wei, W. Guo, A. Pant, X. Xu, J. Shen, L. Ma, D. Hou, Nanostructural origin of semiconductivity and large magnetoresistance in epitaxial $NiCo_2O_4/Al_2O_3$ thin films, J. Phys. D Appl. Phys. 51 (2018) 145308, https://doi.org/10.1088/1361-6463/aab2a3.
[51] A. Mao, F. Quan, H.-Z. Xiang, Z.-G. Zhang, K. Kuramoto, A.-L. Xia, Facile synthesis and ferrimagnetic property of spinel $(CoCrFeMnNi)_3O_4$ high-entropy oxide nanocrystalline powder, J. Mol. Struct. 1194 (2019) 11–18, https://doi.org/10.1016/j.molstruc.2019.05.073.
[52] H. Zhu, H. Xie, Y. Zhao, S. Dai, M. Li, X. Wang, Structure and magnetic properties of a class of spinel high-entropy oxides, J. Magn. Magn Mater. 535 (2021) 168063, https://doi.org/10.1016/j.jmmm.2021.168063.
[53] M. El-Okr, M. Salem, M. Salim, R. El-Okr, M. Ashoush, H. Talaat, Synthesis of cobalt ferrite nano-particles and their magnetic characterization, J. Magn. Magn Mater. 323 (2011) 920–926, https://doi.org/10.1016/j.jmmm.2010.11.069.
[54] L. Fernandez-Barquın, M.V. Kuznetsov, Y.G. Morozov, Q.A. Pankhurst, I.P. Parkin, Combustion synthesis of chromium-substituted lithium ferrites $Li_{0.5}Fe_{2.5-x}Cr_xO_4$ ($x \leq 2.0$): Rietveld analysis and magnetic measurements, Int. J. Inorg. Mater. 1 (1999) 311–316, https://doi.org/10.1016/S1466-6049(99)00045-8.
[55] W. Li, Z. Yu, Q. Wen, Y. Feng, B. Fan, R. Zhang, R. Riedel, Ceramic-based electromagnetic wave absorbing materials and concepts towards lightweight, flexibility and thermal resistance, Int. Mater. Rev. (2023), https://doi.org/10.1080/09506608.2022.2077028.
[56] H. Niu, X. Jiang, Y. Xia, H. Wang, R. Zhang, H. Li, B. Fan, Y. Zhou, Construction of hydrangea-like core–shell $SiO_2@Ti_3C_2T_x$@CoNi microspheres for tunable electromagnetic wave absorbers, J. Adv. Ceram. 12 (2023) 711–723, https://doi.org/10.26599/JAC.2023.9220714.
[57] M.S. Ansari, K.M. Batoo, S. Mehraj, Structural and dielectric properties of Ni-Cu-Mg nanoferrites, in: AIP Conference Proceedings, American Institute of Physics, 2012, pp. 375–376.
[58] M.M. Haque, M. Huq, M. Hakim, Densification, magnetic and dielectric behaviour of Cu-substituted Mg–Zn ferrites, Mater. Chem. Phys. 112 (2008) 580–586, https://doi.org/10.1016/j.matchemphys.2008.05.097.
[59] D. Mandal, K. Mandal, Tuning of structural, magnetic and dielectric properties of TFe_2O_4 (T= Mn, Fe, Co, Ni, Cu, and Zn) Nano-Hollow Spheres: effect of cation substitution, J. Alloys Compd. 851 (2021) 156898, https://doi.org/10.1016/j.jallcom.2020.156898.
[60] R. Tang, C. Jiang, W. Qian, J. Jian, X. Zhang, H. Wang, H. Yang, Dielectric relaxation, resonance and scaling behaviors in $Sr_3Co_2Fe_{24}O_{41}$ hexaferrite, Sci. Rep. 5 (2015) 13645, https://doi.org/10.1038/srep13645.
[61] H. Luo, R. Gong, X. Wang, Y. Nie, Y. Chen, V.G. Harris, Fe_3O_4 cladding enhanced magnetic natural resonance and microwave absorption properties of $Fe_{0.65}Co_{0.35}$ alloy flakes, J. Alloys Compd. 646 (2015) 345–350, https://doi.org/10.1016/j.jallcom.2015.05.208.
[62] Z. Ma, Q. Liu, J. Yuan, Z. Wang, C. Cao, J. Wang, Analyses on multiple resonance behaviors and microwave reflection loss in magnetic Co microflowers, Phys. Status. Solidi. (b) 249 (2012) 575–580, https://doi.org/10.1002/pssb.201147382.
[63] Y. Liu, T. Cui, T. Wu, Y. Li, G. Tong, Excellent microwave-absorbing properties of elliptical Fe_3O_4 nanorings made by a rapid microwave-assisted hydrothermal approach, Nanotechnology 27 (2016) 165707, https://doi.org/10.1088/0957-4484/27/16/165707.
[64] X. Liu, D. Geng, H. Meng, P. Shang, Z. Zhang, Microwave-absorption properties of ZnO-coated iron nanocapsules, Appl. Phys. Lett. 92 (2008), https://doi.org/10.1063/1.2919098.
[65] X. Jiang, H. Niu, J. Li, M. Li, C. Ma, R. Zhang, H. Wang, H. Lu, H. Xu, B. Fan, Construction of core-shell structured $SiO_2@MoS_2$ nanospheres for broadband electromagnetic wave absorption, Appl. Surf. Sci. 628 (2023) 157355, https://doi.org/10.1016/j.apsusc.2023.157355.
[66] L. Song, C. Wu, Q. Zhi, F. Zhang, B. Song, L. Guan, Y. Chen, H. Wang, R. Zhang, B. Fan, Multifunctional SiC aerogel reinforced with nanofibers and nanowires for high-efficiency electromagnetic wave absorption, Chem. Eng. J. 467 (2023) 143518, https://doi.org/10.1016/j.cej.2023.143518.
[67] H. Niu, X. Jiang, W. Li, Z. Min, B.R. Putra, W.T. Wahyuni, H. Wang, R. Zhang, B. Fan, Enhanced electromagnetic wave absorption via optical fiber-like PMMA@$Ti_3C_2Tx@SiO_2$ composites with improved impedance matching, Nano Res. (2023) 1–11, https://doi.org/10.1007/s12274-023-6198-5.
[68] C. Wu, F. Zhang, Q. Zhi, B. Song, Y. Chen, H. Wang, R. Zhang, H. Li, B. Fan, From binary to ternary and back to binary: transition of electromagnetic wave shielding to absorption among MAB phase Ni_3ZnB_2 and corresponding binary borides $Ni_{n+1}B_n$ ($n = 1, 3$), J. Adv. Ceram. 12 (2023) 2101–2111, https://doi.org/10.26599/JAC.2023.9220812.
[69] L. Song, Y. Duan, J. Liu, H. Pang, Insight into electromagnetic absorbing performance of MnO_2 from two dimensions: Crystal structure and morphology design, Mater. Char. 163. https://doi.org/10.1016/j.matchar.2020.110300..
[70] R.F. Zhuo, L. Qiao, H.T. Feng, J.T. Chen, D. Wu, Z.G. Yan, P.X. Yan, Microwave absorption properties and the isotropic antenna mechanism of ZnO nanotrees, J. Appl. Phys. 104 (2008) 119, https://doi.org/10.1063/1.2973198.
[71] Li Xi, Y. Yang, Ultrawide band microwave absorption properties of ultrasound processed CrO_2–paraffin wax composites, Jpn. J. Appl. Phys. 50 (2011), https://doi.org/10.1143/JJAP.50.035805, 35805-35805.
[72] S. Wang, H. Ren, W. Lian, J. Wang, L.B. Kong, Purification and dissociation of raw palygorskite through wet ball milling as a carrier to enhance the microwave absorption performance of Fe_3O_4, Appl. Clay Sci. 200 (2020) 105915, https://doi.org/10.1016/j.clay.2020.105915.
[73] D. Mandal, A. Gorai, K. Mandal, Electromagnetic wave trapping in $NiFe_2O_4$ nano-hollow spheres: an efficient microwave absorber, J. Magn. Magn Mater. 485 (2019) 43–48, https://doi.org/10.1016/j.jmmm.2019.04.033.
[74] F.H. Mohammadabadi, S.M. Masoudpanah, S. Alamolhoda, H.R. Koohdar, Electromagnetic microwave absorption properties of high entropy spinel ferrite ($(MnNiCuZn)_{1-x}Co_xFe_2O_4$)/graphene nanocomposites, J. Mater. Res. Technol. (2021), https://doi.org/10.1016/j.jmrt.2021.07.018.
[75] W. Zhang, H. Xiang, F.Z. Dai, B. Zhao, S.J. Wu, Y. C Zhou, Achieving ultra-broadband electromagnetic wave absorption in high-entropy transition metal carbides (HE TMCs), J. Adv. Ceram. 11 (2022) 11, https://doi.org/10.1007/s40145-021-0554-2.
[76] W. Zhang, F.Z. Dai, H. Xiang, B. Zhao, X. Wang, N. Ni, R. Karre, S.J. Wu, Y. C Zhou, Enabling highly efficient and broadband electromagnetic wave absorption by tuning impedance match in high-entropy transition metal diborides ($HETMB_2$), J. Adv. Ceram. 10 (2021) 1299–1316, https://doi.org/10.1007/s40145-021-0505-y.
[77] W. Zhang, B. Zhao, H. Xiang, F.Z. Dai, S.J. Wu, Y. C Zhou, One-step synthesis and electromagnetic absorption properties of high entropy rare earth hexaborides (HE REB_6) and high entropy rare earth hexaborides/borates (HE REB_6/HE $REBO_3$) composite powders, J. Adv. Ceram. (2021), https://doi.org/10.1007/s40145-020-0417-2.